

On the Use of InSAR for Estimating Timing Errors in Harmonie-Arome Water Vapor Fields

Mulder, Gert; Barkmeijer, Jan; de Haan, Siebren; van Leijen, Freek; Hanssen, Ramon

DOI

[10.1029/2023JD040566](https://doi.org/10.1029/2023JD040566)

Publication date

2024

Document Version

Final published version

Published in

Journal of Geophysical Research: Atmospheres

Citation (APA)

Mulder, G., Barkmeijer, J., de Haan, S., van Leijen, F., & Hanssen, R. (2024). On the Use of InSAR for Estimating Timing Errors in Harmonie-Arome Water Vapor Fields. *Journal of Geophysical Research: Atmospheres*, 130(1), Article e2023JD040566. <https://doi.org/10.1029/2023JD040566>

Important note

To cite this publication, please use the final published version (if applicable).
Please check the document version above.

Copyright

Other than for strictly personal use, it is not permitted to download, forward or distribute the text or part of it, without the consent of the author(s) and/or copyright holder(s), unless the work is under an open content license such as Creative Commons.

Takedown policy

Please contact us and provide details if you believe this document breaches copyrights.
We will remove access to the work immediately and investigate your claim.

On the Use of InSAR for Estimating Timing Errors in Harmonie-Arome Water Vapor Fields

Gert Mulder^{1,2} , Jan Barkmeijer², Siebren de Haan², Freek van Leijen¹, and Ramon Hanssen¹ 

¹Department of Geoscience and Remote Sensing, Delft University of Technology, Delft, The Netherlands, ²Royal Netherlands Meteorological Institute (KNMI), De Bilt, The Netherlands

Key Points:

- Interferometric satellite radar can provide snap shots of high-resolution water vapor fields
- Water vapor fields from numerical weather prediction models can be matched with satellite radar data by time-shifting the model
- Applying time-shifts can lead to model improvements of up to 40%, especially in cases where weather fronts are present

Correspondence to:

G. Mulder,
g.mulder-1@tudelft.nl

Citation:

Mulder, G., Barkmeijer, J., de Haan, S., van Leijen, F., & Hanssen, R. (2025). On the use of InSAR for estimating timing errors in Harmonie-Arome water vapor fields. *Journal of Geophysical Research: Atmospheres*, 130, e2023JD040566. <https://doi.org/10.1029/2023JD040566>

Received 6 DEC 2023

Accepted 3 DEC 2024

Author Contributions:

Conceptualization: Gert Mulder

Data curation: Gert Mulder

Formal analysis: Gert Mulder

Funding acquisition: Ramon Hanssen

Investigation: Gert Mulder

Methodology: Gert Mulder,

Jan Barkmeijer, Siebren de Haan,

Ramon Hanssen

Resources: Gert Mulder, Jan Barkmeijer,

Siebren de Haan

Software: Gert Mulder, Siebren de Haan

Supervision: Freek van Leijen,

Ramon Hanssen

Validation: Gert Mulder

Visualization: Gert Mulder,

Ramon Hanssen

Writing – original draft: Gert Mulder,

Jan Barkmeijer, Freek van Leijen,

Ramon Hanssen

Writing – review & editing: Gert Mulder,

Freek van Leijen, Ramon Hanssen

Abstract Due to its sensitivity to water vapor, high resolution, and global availability, interferometric satellite radar (InSAR) has a large but unexploited potential for the improvement of regional NWP models. A relatively straightforward approach is to exploit the exact instantaneous character of the InSAR data in data assimilation to improve the timing of NWP model realizations. Here we show the potential impact of InSAR data on the NWP model timing and subsequently on improved model performance. By time-shifting the model to find the best match with the InSAR data we show that we can achieve a model error reduction (one-sigma) of up to 40% in cases where weather fronts are present, while other cases show more modest improvements. Most model performance gain due to time-shifts can therefore be achieved in cases where weather fronts are present over the study area. The model-timing errors related to the maximum model error reduction for these cases are in the order of ~ 30 min.

Plain Language Summary Due to its strong sensitivity to water vapor, high resolution, and global availability, interferometric satellite radar (InSAR) has a large but unexploited potential for the improvement of numerical weather prediction (NWP) models. Here we show the potential improvement of NWP models when these models are shifted in time to match the water vapor patterns in InSAR measurements at satellite overpass. This results in model performance increases of up to 40% when weather fronts are present.

1. Introduction

Interferometric synthetic aperture radar (InSAR) is a satellite technique that can be used to estimate water vapor patterns with extreme sensitivity (Hanssen et al., 1999), with a large potential for assimilation in numerical weather prediction (NWP) models (Mateus et al., 2017). Especially the spatial resolution of tens of meters is high compared to conventional meteorological measurements. The launch of the Sentinel-1 satellites provides radar data almost daily with a swath width of 250 km. Therefore, this data source has become very promising for the meteorological community (Hanssen et al., 1999; Mateus et al., 2016) comparable to the commonly used GNSS measurements (Alshawaf et al., 2015; De Haan, 2013; Heublein et al., 2019). Due to its high resolution and high precision InSAR offers a unique measurement unlike other available measurement techniques and can be used to verify water vapor patterns in NWP and reanalysis at satellite overpass. Therefore, Mateus et al. (2018); Miranda et al. (2019); Mateus et al. (2021); Mateus and Miranda (2022) performed case studies where InSAR data is used for data assimilation, but there is currently no systematic or operational use of InSAR in NWP models.

Direct assimilation of InSAR data in NWP models can be challenging due to timing errors in the NWP models, especially when using fixed time windows in assimilation techniques like 3D-VAR (Courtier et al., 1998). Because InSAR provides observations with high resolution water vapor patterns this results in similar patterns of InSAR and NWP model data, but often shifted horizontally due to timing-errors and advection in the model. For example, for a weather front passing over a certain area the NWP model may mis-position the front at a location where it was, for example, an hour ago. Thus, the InSAR measurements and model patterns can be largely the same but shifted in space.

In recent years assimilation techniques like 4D-Var are introduced (Gustafsson et al., 2018), which allow for the use of different observations at their exact observation time instead of using a fixed time for all observations (Barkmeijer et al., 2021; Gustafsson et al., 2018). However, this approach only resolves the time difference between the model analysis and the observation, but it cannot correct for an internal timing error in the model.

© 2024. The Author(s).

This is an open access article under the terms of the [Creative Commons Attribution License](https://creativecommons.org/licenses/by/4.0/), which permits use, distribution and reproduction in any medium, provided the original work is properly cited.

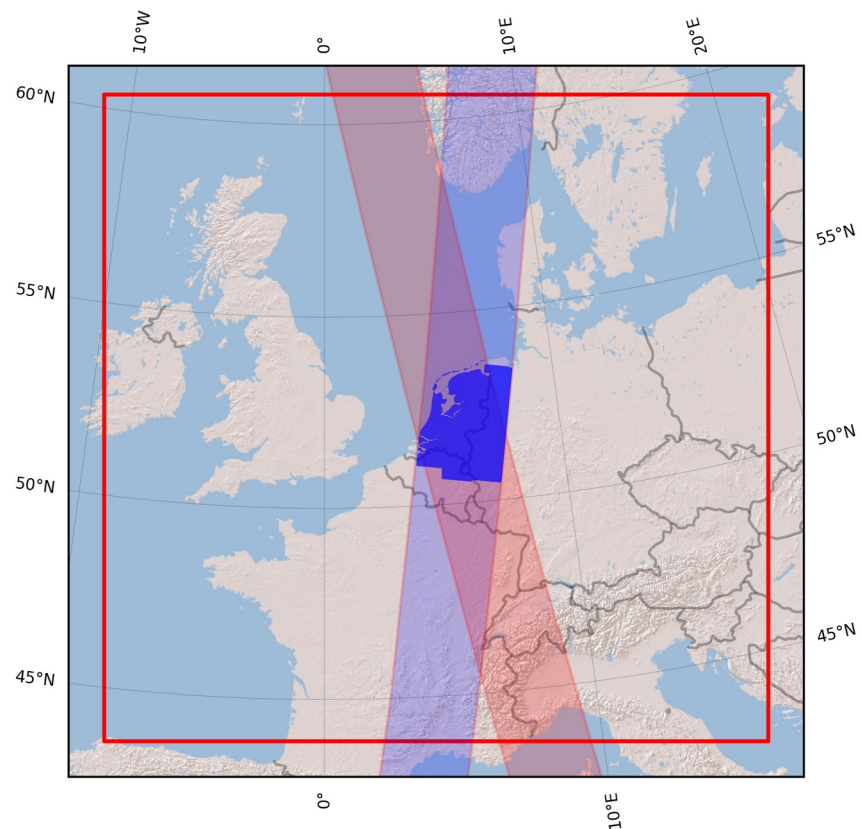


Figure 1. Coverage of the Harmonie-Arome model (red box), the used study area (shaded dark blue area) and the ascending (red shaded area) and descending (blue shaded area) Sentinel-1 tracks over the study area. Water areas are masked out because InSAR measurements over water are unreliable.

Therefore, we argue that the inclusion of InSAR-derived time-shifts in the data assimilation can benefit NWP model performance. In this study we show the potential benefit of using time-shift in data assimilation based on a time-series of Sentinel-1 SAR acquisitions combined with a time-series from the Harmonie-Arome NWP model (Bengtsson et al., 2017) over the Netherlands, see Figure 1. This is done by time-shifting the NWP model using model advection to isolate the effect of timing errors in NWP models based on InSAR data. This provides a straightforward approach that covers almost all cases, although in some cases the assumption of pure advection will cause non-trivial model errors due to dominant non-linear effects. The developed method is therefore not meant to replace any current assimilation method, but shows whether the incorporation of time-shifts within the current frameworks could potentially benefit their performance.

First we show how InSAR measurements relate to meteorological parameters and how single-epoch delays can be estimated from a time-series of InSAR measurements (Mulder et al., 2022) and NWP models, that is, the realizations of the NWP model at a particular time. Then we use NWP model advection to show the influence of timing differences and evaluate the NWP model performance within a time window of 4 hr around the InSAR acquisition time. The difference in performance between different time-shifts is then be used to find the optimal time-shift for the NWP model. Finally, we convert delay values to precipitable water vapor (PWV) values, which are used to find the relative size of the residuals with the total water vapor variations in the model.

2. Methods

In this section we first describe the relation of InSAR tropospheric delays with NWP model parameters and how we can derive equivalent InSAR delays from NWP model data. Then we describe how we derive absolute single-epoch delays and precipitable water vapor (PWV) values and how we can shift the NWP model in time to find the

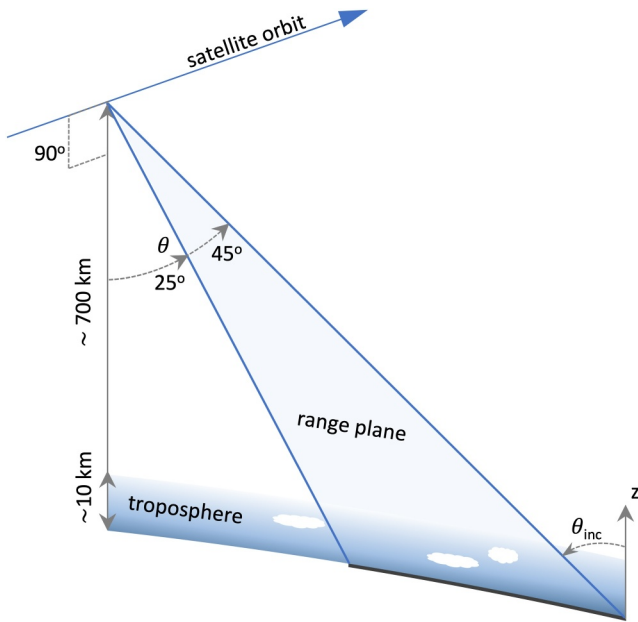


Figure 2. The satellite geometry of the Sentinel-1 satellite mission. The radar signals are transmitted perpendicular to the satellite direction along the range plane, which is also called the zero-Doppler plane. The Sentinel-1 radar observes a swath with a width of about 250 km in IW mode with a range in look-angles θ of approximately 25–45°, which is slightly different from the incidence angle θ_{inc} due to the earth's curvature. The tropospheric delays depend on the pressure, temperature and water vapor along the slant satellite path.

time-shifted delay values. Finally, we describe how the delay differences between single-epoch InSAR and equivalent delays from NWP model are used to estimate the optimal time-shifts.

2.1. Tropospheric Delay in InSAR Measurements

The InSAR atmospheric delay along the signal path, is derived by integrating the refractivity along the slant satellite path (Smith & Weintraub, 1953)

$$\delta = \int_{\text{scat}}^{\text{sat}} N(z) dz, \quad (1)$$

where δ is the one-way signal delay in millimeters, “scat” the location of the radar scatterer on the ground and “sat” the location of the satellite. Figure 2 shows the geometry of the Sentinel-1 observation, which employs a side-looking radar where the radar signal is transmitted and received perpendicular to the satellite path (Yague-Martinez et al., 2016). Refractivity N is modeled as (Smith & Weintraub, 1953)

$$N = k_1 \frac{P}{T} + k_2' \frac{e}{T} + k_3 \frac{e}{T^2} + k_4 \frac{n_e}{f^2} + k_5 W, \quad (2)$$

where T is the temperature in Kelvin, e is the partial pressure of water vapor, P the air pressure, n_e is the electron density per cubic meter, f the radar frequency and W the liquid water content. The values of the constants are $k_1 = 77.6$, $k_2' = 23.3$ and $k_3 = 3.75 \cdot 10^5$, (Thayer, 1974), $k_4 = -4.028 \times 10^7$ and $k_5 = 1.4$. The first term in this equation represents the hydrostatic part and the second and third part the wet part of the tropospheric delay (Ishimaru, 1978). The fourth term represents the ionospheric refractivity, while the fifth term is the liquid water refractivity. From these, the ionospheric part can be modeled accurately (Meyer, 2011) or derived using spectral diversity (Gomba et al., 2016, 2017) and the liquid water refractivity is negligible small for C-band radar (Hanssen, 2001). Note that attenuation of the signal due to liquid water in C-band, see Danklmayer and Chandra (2009), is not relevant for the refractivity and hence the phase delay.

2.2. Equivalent Delays From NWP Model

To evaluate results from NWP model using InSAR-derived tropospheric delays, an equivalent InSAR delay is estimated from the NWP model parameters. This is done using a ray-tracing technique that follows the slant signal path to find the NWP model parameter values in the model grid cells the radar signal passes through (De Haan, 2008), see Equation 1. To do so, pressure P , specific humidity q , and temperature T values are first interpolated onto the zero-Doppler plane to allow ray-tracing in this 2D plane. Based on the slant path within the zero-Doppler plane the (P, T, q) values are interpolated for each model level, which are defined in the model by a top and bottom pressure value. Using Equations 1 and 2 the integrated delay $\delta_{\text{NWP},l}^t$ for every model level l at time t is then calculated (De Haan, 2008),

$$\delta_{\text{NWP},l}^t = \frac{\Delta P_l}{\sin \theta_{\text{inc}}} \left(k_1 \frac{R_d}{g_h} + k_2' \frac{R_v}{g_h} q_l + k_3 \frac{R_v}{g_h T_l} q_l \right), \quad (3)$$

where ΔP_l is the pressure difference between the top and bottom of level l at time t , R_d and R_v are the gas constants for dry and moist air, g_h is the gravity at given height h , θ_{inc} is the incidence angle, T_l is the mean temperature and q_l is the specific humidity at model level l . The model level delay is divided by $\sin \theta_{\text{inc}}$ to compensate for the increased path length of the radar signal through the model layer due to the non-vertical signal path, see Figure 2. Using the integrated delays per model level the total delay follows from summation over all levels,

$$\delta_{\text{NWP}}^t = \sum_{l=1}^n \delta_{\text{NWP},l}^t, \quad (4)$$

where δ_{NWP}^t is the single-epoch delay for n model levels. The estimated average precision (standard-deviation) of the equivalent delays $\sigma_{\delta_{\text{NWP}}^t}$ is ~ 10 mm in winter and ~ 20 mm in summer over the selected study area (Mulder et al., 2022).

2.3. Single-Epoch InSAR Delays

Due to the differential nature of InSAR delays it is only possible to derive a double-difference in delay—between two satellite acquisitions in time and between two points in space. To arrive at “single-epoch” delays we use a time-series of InSAR and equivalent NWP model delays, and a constrained least-squares method to provide an absolute reference to these atmospheric delays, as proposed by (Mulder et al., 2022). The resulting single-epoch delay $\delta_{\text{SAR},p}^t$ is decomposed into

$$\delta_{\text{SAR},p}^t = \delta_{\text{SAR,var,rel},p}^t + \delta_{\text{NWP,cm},p}^t + \delta_{\text{NWP,bias}}^t, \quad (5)$$

where $\delta_{\text{SAR,var,rel},p}^t$ is the spatially variable part of the delay signal (relying on InSAR data), $\delta_{\text{NWP,cm},p}^t$ is the common mode of the signal, which is the average delay value that is present in every single-epoch atmospheric delay and can be derived from the average NWP model equivalent delay values in time. δ_{bias}^t is an image-wide bias value independent of pixel location p that is calculated from InSAR and NWP model. The difference between the InSAR and NWP model data $\Delta\delta_p^t$ can now be given by,

$$\Delta\delta^t = \delta_{\text{NWP}}^t - \delta_{\text{SAR}}^t. \quad (6)$$

because the common mode $\delta_{\text{NWP,cm},p}^t$ is both part of the single-epoch InSAR and NWP model delay, it will cancel out in the differential delay $\Delta\delta_p^t$, eliminating any influence of the common mode on the estimated time-shifts, see also Section 2.7. The used interferograms in our study are derived from a stack of Sentinel-1 acquisitions over the Netherlands. To calculate InSAR delays all the SAR acquisitions are co-registered and resampled based on the Sentinel-1 precise orbits, corrected for the topographic phase based on a DEM, and georeferenced. Then, we use a geographic coordinate system with square grid cells of 500 m and compute the average InSAR phase values for all non-water grid cells, after which the grid is unwrapped. To reliably unwrap the data in 2D it is important that the unwrapped data is spatially contiguous. Therefore, areas which are separated from the main land by large water bodies, for example, the islands in the north of the Netherlands, are excluded from the data. The estimated average precision (standard-deviation) of the InSAR signal per pixel $\sigma_{\delta_{\text{SAR},p}^t}$ is ~ 1 mm in winter and ~ 2 mm in summer over the selected study area (Mulder et al., 2022).

2.4. Precipitable Water Vapor From Single-Epoch InSAR Delays

Although conversion to precipitable water vapor (PWV) is not necessarily needed to track shifts in water vapor fields in InSAR and NWP model data, it is a commonly used variable in meteorology and therefore useful to interpret the delay differences, for example, as shown in Figure 3. PWV is the vertically integrated water vapor for the full troposphere given in millimeters of liquid water and can be related to delay variations over a single-epoch InSAR image (Bevis et al., 1996),

$$\text{PWV}_{\text{SAR}}^t = \delta_{\text{SAR,wet}}^t \sin\theta_{\text{inc}} \Pi^t, \quad (7)$$

where $\Pi \approx 0.15$ (Bevis et al., 1994), and $\delta_{\text{SAR,wet},p}^t$ is the wet part of the SAR tropospheric delay, which is the integrated refractivity of the wet components of Equation 2 along the slant satellite path. $\sin\theta_{\text{inc}}$ is the conversion from the slant path of the delays to the vertical integrated PWV values, similar to Equation 3. The exact value of Π is dependent on the mean temperature of the atmosphere and can vary with about 10%. Yet, it can be derived from NWP model data based on Equations 3 and 4, that is,

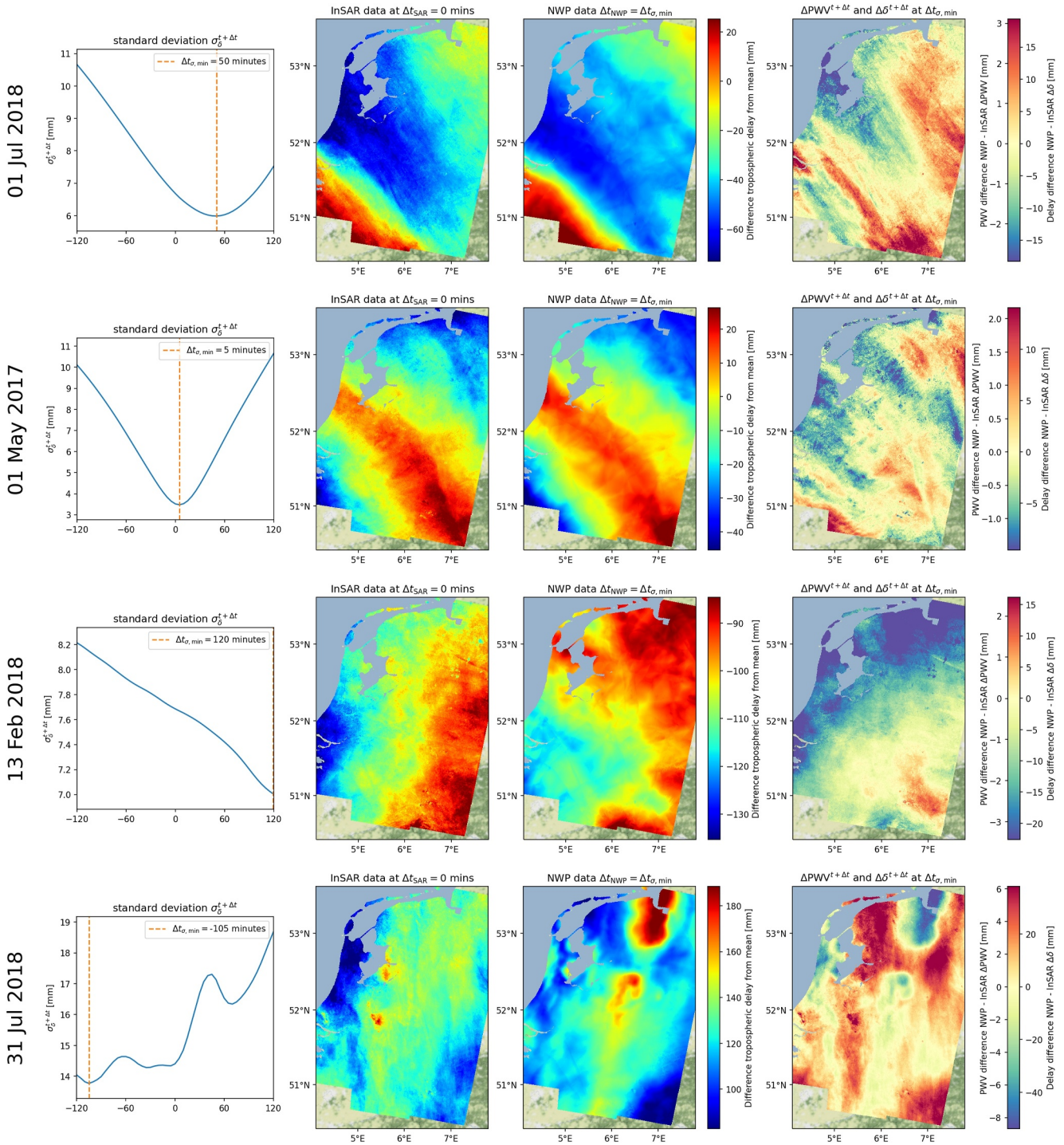


Figure 3. Example of four representative cases for finding the optimal time-shifts $\Delta t'_{min}$. The first column gives the optimization of the $\sigma_{\delta^{t+\Delta t}}^{t+\Delta t}$ function. The second column shows the InSAR delays $\delta_{SAR,var}^t$ and the third column shows the NWP model delays $\delta_{NWP,var}^t$ relative to the mean $\delta_{NWP,cm}^t$ at the optimal time-shift $\Delta t'_{min}$. The last column show the difference between NWP model and InSAR data as delay values $\Delta \delta^{t+\Delta t}$ and PWV values $\Delta PWV^{t+\Delta t}$. The first row shows a case where the time-shift is well determined and $\Delta t_{\sigma} \geq 15$ min ($n = 58$). The second row shows a case which is well determined with $\Delta t_{\sigma} < 15$ min ($n = 38$). The third row gives a case where the patterns between NWP data and InSAR data are too dissimilar, which results in an optimal time-shift outside the $[-120, +120]$ min time domain ($n = 24$). The fourth row shows a case with strong convective systems, which cannot be aligned using a time-shift as it results in multiple local minima in the optimization curve ($n = 20$).

$$\Pi' = \frac{10^6}{\rho R_v (k_3/T_m^t + k_2')}, \quad (8)$$

where ρ is the density of liquid water, R_v is the specific gas constant for water vapor and $T_{m,p}^t$ is the weighted mean temperature of the atmosphere (Davis et al., 1985). Values for $T_{m,p}^t$ can be estimated from NWP model data with a precision of $\sigma_{T_{m,p}^t} = 2.5$ K (Huang et al., 2022), using

$$T_m^t = \frac{\int_{\text{scat}}^{\text{sat}} e^t/T^t dz}{\int_{\text{scat}}^{\text{sat}} e^t/T^{t^2} dz}, \quad (9)$$

where e and T are the water vapor pressure and temperature along the radar signal path between the satellite and scatterer on the ground. By combining the precision of $T_{m,p}^t$ and other contributors to Π this leads to an average precision of $\sigma_{\Pi'} = 0.0015$. Based the estimated value of Π' it is now possible to derive the PWV from wet delay $\delta_{\text{SAR},p,\text{wet}}^t$, but the total InSAR delay $\delta_{\text{SAR},p}^t$ also contains a hydrostatic component $\delta_{\text{NWP},p,\text{hyd}}^t$, which is integrated refractivity of the first component of Equation 2. The wet component is therefore derived by subtracting the estimated hydrostatic component from the NWP model from the total InSAR delay,

$$\delta_{\text{SAR},\text{wet}}^t = \delta_{\text{SAR}}^t - \delta_{\text{NWP},\text{hyd}}^t, \quad (10)$$

where $\delta_{\text{NWP},p,\text{hyd}}^t$ is the absolute hydrostatic delay from NWP data. Although in Equation 2 the hydrostatic refractivity is dependent on pressure and temperature, it is only dependent on pressure when rewritten to integrated delays, see Equation 3, and can accurately be estimated based on surface pressure only (Elgered et al., 1991). Given that surface pressure only varies smoothly and in-situ surface pressure measurements used in the used NWP model have a precision of $\sigma_{p_s} = 0.3$ hPa (WMO, 2018) this leads to an estimated precision of NWP model derived hydrostatic delay of $\sigma_{\delta_{\text{NWP},\text{hyd}}^t} = 0.7$ mm for the used Harmonie model. After subtracting single-epoch InSAR and equivalent NWP model delays, the hydrostatic part will therefore largely cancel out and the remaining horizontal delay variations are almost entirely due to differences in wet delay. This means that these delay differences can be expressed in both delay difference $\Delta\delta^t$ and PWV differences ΔPWV^t , which are linearly related by the factor Π' , see column four in Figure 3.

2.5. NWP Model Time-Shifts

The most apparent method to apply NWP model time-shifts would be to evaluate the NWP model delay at different moments in time, in which case model advection but also non-linear effects and changes in the boundary layer would be well-represented. However, this would introduce unwanted changes in temperature and radiation values due to diurnal variations, while we want to keep the time of the day fixed at the satellite overpass time over the whole time window. Consequently, this would also have unwanted consequences for the water vapor variations due to for example, changing air temperatures, evaporation and transpiration on the ground and/or growth of the boundary layer. Therefore, we will only use a single evaluation of the NWP model closest to the satellite overpass and adjust the water vapor, temperature, and pressure fields using advection only. This does prevent the effect of diurnal variations and also gives a more accurate description of the movement of water vapor patterns. Because vertical air movement is generally small compared to horizontal air movement, we disregard them, such that the advection due to time-shifts can be calculated for individual model levels. Although in specific cases this will cause significant errors in the time-shifted model, this will not outweigh the unwanted diurnal effect in most other cases. Therefore, time-shift estimates for cases with significant non-linear effects and/or boundary layer changes will be unreliable.

The shift in location of an air parcel for every time step dt for all model layers l is then derived from the horizontal wind speeds u and v by

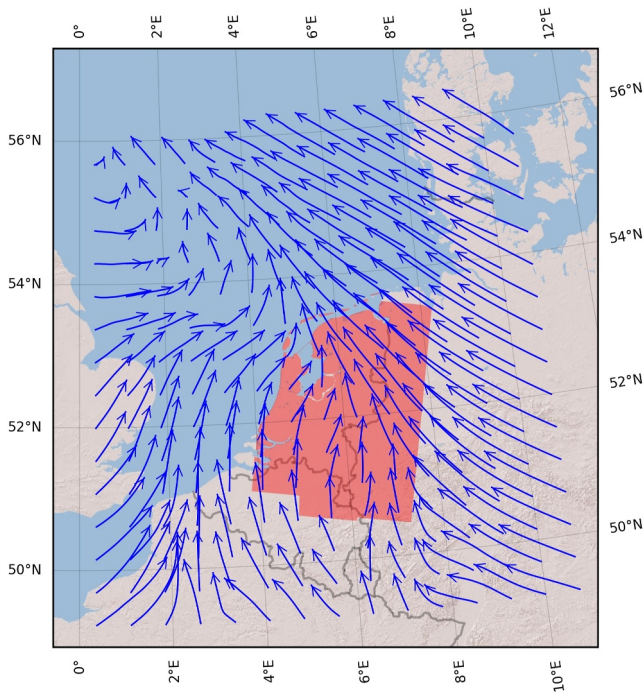


Figure 4. Example of the horizontal movement of air parcels due to time-shifts for one model realization at one vertical model level. The movement of individual air parcels are shown as blue arrows and the used study area over the Netherlands is given in red. This shows the diversity of directions and distances traveled of air parcels over a time span of 120 min.

$$\begin{aligned} x^{t+\Delta t} &= x^t + u^t(x^t, y^t) dt, \\ y^{t+\Delta t} &= y^t + v^t(x^t, y^t) dt, \end{aligned} \quad (11)$$

where x^t (e.g., east) and y^t (e.g., north) are the horizontal coordinates of an air parcel with its own temperature and specific humidity value in model layer l for time t . $u^t(x^t, y^t)$ and $v^t(x^t, y^t)$ are the wind speeds at time t in the x and y direction, respectively. To find the shift in coordinates at time-shift Δt , Equation 11 is applied recursively n times with time steps dt of 5 min, so $\Delta t = n dt$. (Smaller values of dt yield only minimal location changes in x and y , especially for cases with large wind shear.) Figure 4 gives an example of the resulting path of air parcels, leading to a horizontal shift in space driven by a shift in time. Using the results from Equation 11 pressure P , temperature T , and specific humidity q fields can then be shifted in time by applying a shift in space due to advection, assuming no diurnal effects, friction and energy dissipation, per model layer:

$$\begin{aligned} T^{t+\Delta t}(x, y) &= T^t(x^{t+\Delta t}, y^{t+\Delta t}), \\ P^{t+\Delta t}(x, y) &= P^t(x^{t+\Delta t}, y^{t+\Delta t}), \\ q^{t+\Delta t}(x, y) &= q^t(x^{t+\Delta t}, y^{t+\Delta t}), \end{aligned} \quad (12)$$

where the values of temperature T , pressure P and specific humidity q at locations x^t and y^t are derived using bi-linear interpolation at model level. After applying Equation 12 for all model levels l the single-epoch InSAR equivalent delay values are then derived using Equations 3 and 4 for different NWP model time-shifts Δt . This gives us a time-series of acquisitions for equivalent NWP model delay as a function of Δt , which are directly comparable with single-epoch InSAR atmospheric delays, see Figure 3.

2.6. Resolution Differences Between InSAR and NWP Model Data

When comparing NWP model and InSAR data, it is important to evaluate both data sets at the same spatial resolution because the differences between both may also be caused by resolution differences. The used Sentinel-1 InSAR data was processed with a resolution of 500 m, while the NWP model resolution is about 2.5 km. However, the effective resolution at which the model can represent atmospheric phenomena is about seven times the grid resolution for meso-scale NWP models (Skamarock, 2004), that is, a resolution of 17.5 km. Because the effective resolution can vary due to the model setup or study area, we approximate the effective resolution independently using the spectrum of both the InSAR and NWP model data. To find the effective resolution, the resolution of the InSAR data is reduced for different resolutions using a uniform filter until the spectra from InSAR and NWP model data match. Figure 5 gives an example of the 500 m InSAR results, the NWP model data, and the filtered InSAR data. This leads to an effective resolution of the used Harmonie-Arome model of 12.5 km which is used for the size of a uniform filter to reduce the InSAR resolution, leaving out all water pixels.

2.7. Description of NWP Model Error

To estimate the NWP model performance for all time-shifts Δt , the standard deviation $\sigma_{\delta}^{t+\Delta t}$ of the difference between single-epoch InSAR delays and time-shifted equivalent NWP delays is used. Because the typical NWP model

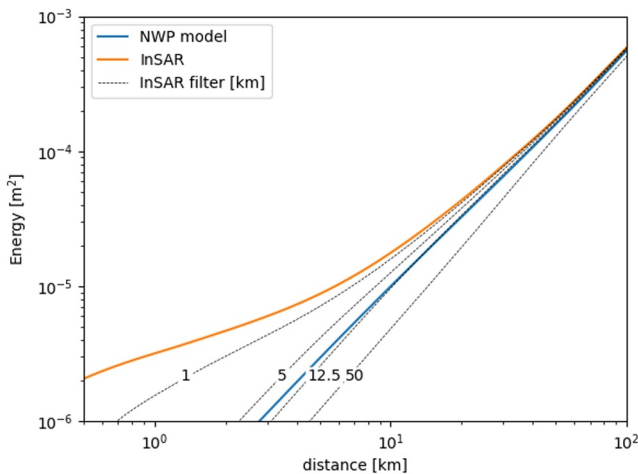


Figure 5. Comparison of the structure function of the variable part of the delays derived from NWP model and the InSAR-derived atmospheric delays for one particular epoch, representative for most of the time-series. This shows that for the smaller distances of up to ~ 15 km, the InSAR data contain more energy than the NWP data, which shows the potential of InSAR data to improve high-resolution NWP model analyses. Applying a uniform filter of 12.5 km on the InSAR data aligns the power spectra, indicating that the information content corresponds with that of the NWP model.

error is an order of magnitude larger than the InSAR delay error (Mulder et al., 2022), we assume that the errors in the InSAR measurement are not significant in the estimation of $\sigma_{\delta}^{t+\Delta t}$. Therefore, $\sigma_{\delta}^{t+\Delta t}$ can be used as an estimate of the NWP model error.

The standard deviation is selected because it relates closely to the applied least-squares methods in the assimilation, making it a suitable variable to measure model errors. Further, it only relies on the variability of InSAR and NWP model differences, which eliminates any influence of the NWP model common mode $\delta_{\text{NWP,cm},p}$, see Section 2.3, contrary to for example, the root mean squared error (RMSE). Finally, it is not influenced by the estimated bias δ_{bias}^t between the InSAR and NWP model data as it centers around the mean, eliminating the dependence on NWP model data in the single-epoch estimate δ_{SAR}^t .

First the difference between the InSAR and NWP model data at time t at a time-shift Δt is defined by,

$$\Delta\delta^{t+\Delta t} = \delta_{\text{NWP}}^{t+\Delta t} - \delta_{\text{SAR}}^t, \quad (13)$$

where $\delta_{\text{NWP}}^{t+\Delta t}$ is the time-shifted NWP model data and δ_{SAR}^t is the single-epoch InSAR delay. The standard deviation is defined by

$$\sigma_{\delta}^{t+\Delta t} = \sqrt{\frac{\sum_{p=0}^n \left(\Delta\delta_p^{t+\Delta t} - \overline{\Delta\delta}^{t+\Delta t} \right)^2}{n}}, \quad (14)$$

where $\sigma_{\delta}^{t+\Delta t}$ is the standard deviation of the difference between InSAR and NWP atmospheric delay values for all pixels p at epoch t and time-shift Δt . To estimate the standard deviation all the pixels over the sea, rivers and other inland water bodies were excluded because InSAR delay measurements are not possible over these areas. Similarly, also the model performance for PWV values can be given based on the difference between InSAR and NWP model data by,

$$\Delta\text{PWV}^t = \Delta\delta^{t+\Delta t} \Pi^{t+\Delta t}, \quad (15)$$

where ΔPWV^t is the difference in PWV and $\Pi^{t+\Delta t}$ the derived conversion factor from Section 2.4. The standard deviation of PWV,

$$\sigma_{\text{PWV}}^{t+\Delta t} = \sqrt{\frac{\sum_{p=0}^n \left(\Delta\text{PWV}_p^{t+\Delta t} - \overline{\Delta\text{PWV}}^{t+\Delta t} \right)^2}{n}}, \quad (16)$$

where $\sigma_{\text{PWV}}^{t+\Delta t}$ is the standard deviation of the differences between InSAR and NWP model data PWV values.

2.8. Selection Optimal Time-Shifts

Based on the standard deviation $\sigma_{\delta}^{t+\Delta t}$ for all different time-shifts Δt , the optimal time-shift Δt_{min}^t is defined as the time-shift where the standard deviation is lowest. The selected search space for Δt to find an optimal value is $[-120, +120]$ min, with a time resolution of 5 min,

$$\Delta t_{\text{min}}^t = \underset{\Delta t}{\text{argmin}} \{ \sigma_{\delta}^{t+\Delta t} \}, \text{ for } \Delta t \in [-120, 120], \quad (17)$$

where Δt_{min}^t is the time-shift in minutes with the lowest standard deviation. The selected time window is a trade-off between maximizing the search space to find an optimal time-shift and the validity of the assumption made in Section 2.5 for larger time spans. Therefore, we choose a time window of $[-120, +120]$, which is somewhat larger than the assimilation time window $[-120, +60]$ used in 4D-Var assimilation in the Harmonie model (Barkmeijer et al., 2021).

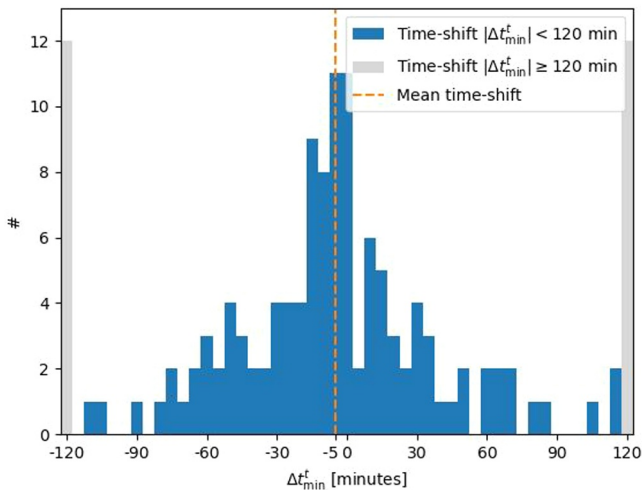


Figure 6. Distribution of best fit in time over a $[-120, 120]$ min window around NWP model analysis time at 6:00 UTC. $\sim 80\%$ of all SAR acquisitions give a useful indication of the time differences, while the remaining 20% has no clear optimum in the given time window. The mean time-shift is -5 min, which is likely due to satellite overpass time at 5:50 UTC, which is 10 min before the NWP model analysis time.

3. Results and Discussion

In this section we evaluate the performance of the NWP model time-shift. First we describe the used data sets and show the results of four representative cases. Second, we convert the delay differences between InSAR and NWP model data to PWV differences. Then we discuss the relation between the retrieved time-shifts and the model error reductions, given seasonal differences and specific weather situations.

3.1. Model Inputs and Study Area

We use time series of 140 Sentinel-1 SAR acquisitions (descending track 37, at 5:50 UTC, in VV polarization) and NWP model data over the Netherlands between 2016 and 2018. This yields a stack of InSAR atmospheric delay values with a 500 m resolution as described in 2.3. We use the Harmonie-Arome NWP model (Bengtsson et al., 2017), which is the operational weather model for the Netherlands. The horizontal resolution is about 2.5 km and it consists of 65 vertical model levels. The spatial coverage of the model realizations for this study is about 2000×2000 km centered at the Netherlands and nested within the operational ECWMF global model (Palmer, 2019), see Figure 1. NWP model delays are then derived for every InSAR pixel, using a ray-tracing method that follows the slant satellite path through NWP model grid, see Section 2.2.

3.2. Optimal Time-Shifts NWP Models

The rows of Figure 3 show the results for four representative cases in time-shift estimation. The first column shows the standard deviation $\sigma_{\delta}^{t+\Delta t}$ of the difference between InSAR and NWP model as a function of time, with the optimal time-shift Δt_{\min}^t indicated by the dashed line (see Sections 2.7 and 2.8). The second column shows the single-epoch InSAR delays $\delta_{\text{SAR,var},p}^t$ and the third column shows the equivalent NWP model delays $\delta_{\text{NWP,var},p}^{t+\Delta t}$ at time-shift $\Delta t = \Delta t_{\min}^t$. Note that the second and third column show only the variable part of the delay, that is, without the common mode $\delta_{\text{NWP,cm},p}$, leading to delay values up to a few hundred mm above or below the average delay value of about 2.45 m (Mulder et al., 2022). The last column shows the difference between single-epoch InSAR and equivalent NWP delay data, which is expressed in terms of delay and PWV differences.

The first row in Figure 3 shows a situation with a significant time-shift of about 1 hr, which occurs in about 58 of the total 140 cases (41%). The second row shows a similar case where the timing with an optimal time-shift within the $[-10, 10]$ min interval, which only leads to marginal model error reduction. Similar results with small time-shifts and marginal model error reductions are found for 38 out of the total 140 cases (27%). The third row shows a case with an optimal time-shift of 120 min, indicating that the optimal time-shift is outside the $[-120, 120]$ min interval, and time-shift should therefore not be used for similar cases. Often this is related to cases with small delay differences or cases where the delay patterns in the NWP and InSAR data are very dissimilar due to low NWP model or InSAR data quality. This occurs in 24 of the total 140 cases (17%). The last row shows a case where most delay variation is caused by local convective weather cells, which is predicted by the NWP model, but not at the correct location and with a different size, which is as expected in cases of local convection. This leads to a wrong time-shift estimate, because the development of convective systems cannot be related to advection only, but is also dependent on non-linear effects and boundary layer changes. It is therefore not possible to align the convective systems in the model and InSAR data using a time-shift and a time-shift should not be applied in these cases. Fortunately, these cases can easily be identified as they show multiple minima in the optimization curves and flagged as unreliable. In this study this was the case for 20 of the total 140 epochs (14%).

The distribution of the optimal time-shift for all 140 acquisitions is given in Figure 6. It is centered around -5 min with most values between -60 and $+60$ min. For 24 epochs an optimal time-shift could not be found within the $[-120, 120]$ window and are indicated in gray. The standard deviation of the optimal time-shifts after removal of these cases is about 30 min. The mean time-shift of -5 min is likely related to the overpass time of the InSAR satellite at 5:50 UTC while the NWP model analysis is at 6:00 UTC.

3.3. Magnitude of Model Error

To describe the NWP model error, presuming the InSAR delays represent the truth, we use the standard deviation of the difference between InSAR and NWP model delay values per scene $\sigma_{\delta}^{t+\Delta t}$. This does provide a metric in order to find the optimal time-shift. Yet, it does not give an indication of how large this NWP model error is relative to the actual total water vapor variability per scene. We decided to analyze this in terms of PWV instead of delay. We convert the NWP model error to PWV values, $\sigma_{\text{PWV}}^{t+\Delta t}$ (cf. Section 2.4) and then compare this to the total variability of PWV per scene, using

$$\text{var}_{\text{PWV}}^t = \sqrt{\frac{\sum_{p=0}^n (\text{PWV}_{\text{NWP},p}^t - \overline{\text{PWV}}^t)^2}{n}}, \quad (18)$$

where $\text{var}_{\text{PWV}}^t$ is a scalar metric for the variability of the PWV signal for the scene at time t , and $\text{PWV}_{\text{NWP},p}^t$ are the PWV values from the NWP model for all pixels p in the scene. To find the relative size of the model error compared to the total water vapor variability the signal-to-noise ratio (SNR) of the NWP model is

$$\text{SNR}^t = \frac{\text{var}_{\text{PWV}}^t}{\sigma_{\text{PWV}}^t}, \quad (19)$$

where SNR^t is the ratio of the variability of the PWV in the scene, dependent on the actual weather situation (the signal), and the error in the NWP model (the noise). Figure 7a shows the seasonal variability of the total variation in PWV per scene $\text{var}_{\text{PWV}}^t$ (in blue) and (ii) the NWP model error per scene σ_{PWV}^t (in orange). Both variables show a clear seasonal signal: higher in summer and lower in winter. This is likely due to the differences in mean temperature T_m^t , which directly influence the maximum possible water vapor pressure e_{max}^t (Alduchov & Eskridge, 1997) and, hence, PWV. Figure 7b gives the SNR as discussed above. This shows that the NWP model errors are a significant fraction of the actual signal, that is, more than about 25% ($\text{SNR}^t < 4$) of the signal for most weather situations. In some cases the NWP model error is even larger than the variability at that weather situation, resulting in $\text{SNR}^t < 1$. This implies that although the NWP model can give a good description of the weather type, the localization of specific weather features within the InSAR swath-width of 250 km is sub-optimal, leading to large errors in the numerical weather model.

3.4. Model Error Reduction Due To Time-Shifts

The reduction of the model error due to time-shifts $g^{t+\Delta t_{\text{min}}}$ is given as a fraction of the delay difference between InSAR and NWP model data,

$$r_e^{t'} = 1 - \frac{\sigma_{\Delta\delta}^{t'}}{\sigma_{\Delta\delta}^t}, \quad \text{with } t' = t + \Delta t_{\text{min}}^t, \quad (20)$$

where the numerator and the denominator are the delay difference after and before time-shift correction, respectively. Thus, the reduction $r_e^{t'}$ is the percentage wise improvement due to applying the time shift, see Figure 8a. Figure 8b shows the relative model error reduction $r_e^{t'}$ in relation to the absolute time-shift $|\Delta t_{\text{min}}^t|$. We expect that a larger time shift will lead to a larger spatial shift, and therefore a larger error reduction. The estimated trend line suggests a model error reduction of 0.19% for every minute the NWP model is time-shifted, up to ~15% reduction for a 90 min time shift. Yet, the actual error reduction varies greatly for different weather situations with the same optimal time-shift. A small number of cases shows error reductions up to 40%, even with relatively small time-shifts. This indicates that there are specific weather conditions where time-shifts have a strong impact on model performance. Note that larger time-shifts will be less reliable, since friction, dissipation, and vertical transport will start to become more important.

The color of the dots in Figure 8b represent the SNR values SNR^t . To determine whether SNR values have an influence on the model error reduction the dots in Figure 8b are divided in a set with high SNR values ($\text{SNR}^t > 2$) and low SNR values ($\text{SNR}^t < 2$) and fitted as dashed lines. This shows that high SNR values ($\text{SNR}^t > 2$) have an

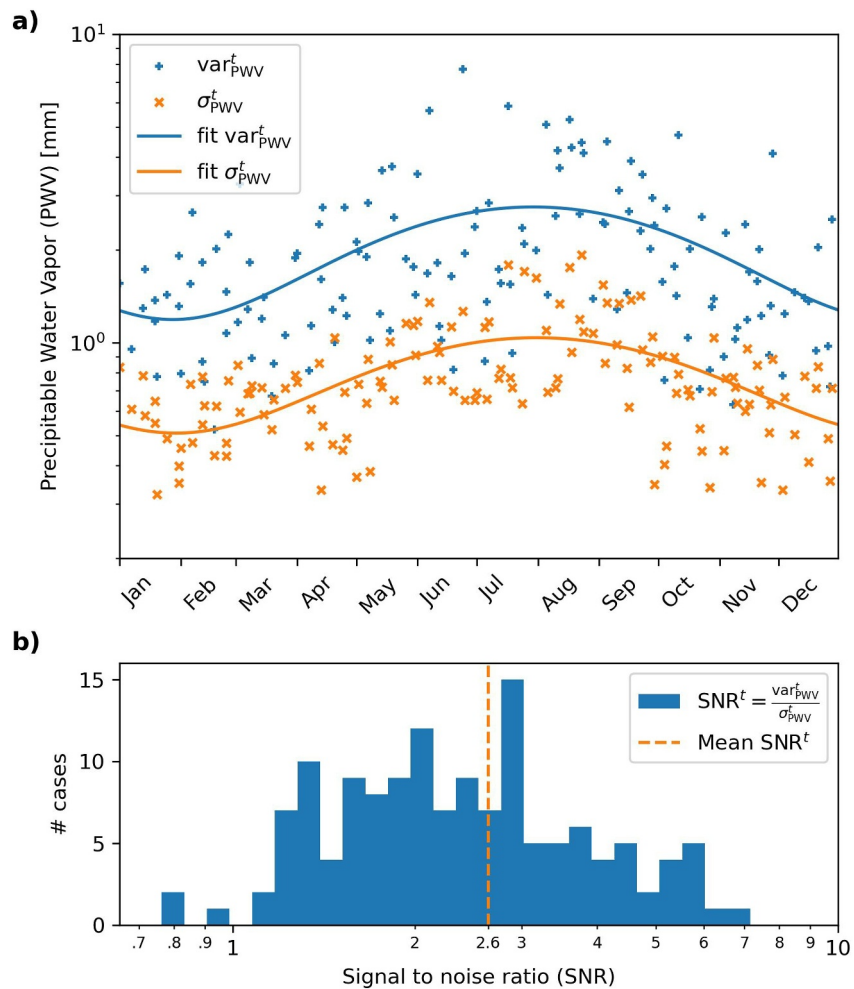


Figure 7. PWV values and precision of NWP model data. (a) Seasonal cycle of the variability of PWV values $\text{var}_{\text{PWV}}^t$ (in blue) and the variability of the NWP model error (in orange). Both data sets show a seasonal cycle with highest values in summer, which can be related to higher absolute humidity values due to higher temperatures. (b) Signal-to-noise ratio (SNR) for NWP model SNR^t, which shows that the NWP model error (noise) is large compared to the variability of NWP model PWV over the scene (signal).

average model error reduction of 0.24% per minute time-shift and the lower SNR values ($\text{SNR}^t < 2$) an average model error reduction of 0.15% per minute time-shift. This means that the model error reduction is larger in cases where the NWP model already describes the water vapor field relatively well. This is likely because the water vapor patterns from InSAR and NWP model data should already be relatively similar before the application of a time-shift is effective. For example, in the third case of Figure 3 the water vapor patterns are too dissimilar to effectively apply a time-shift, while for the first two cases a clear improvement can be found as the patterns of the InSAR and NWP model data are much more similar.

3.5. Model Error Reduction With Different Weather Types

Based on the analyzed cases in this study we can now evaluate the applicability of time-shifts based on seasonality and weather type. Figure 9 shows the NWP model error per epoch σ_{δ}^t without time-shift in blue and with time-shift in orange, with orange lines highlighting the level of improvement. This shows that there is a clear seasonality of the total model error σ_{δ}^t , likely related to higher variations in temperature and specific humidity values during the summer season (KNMI, 2023a). However, there is no clear seasonality in the reductions of the model errors due to the applied time-shifts.

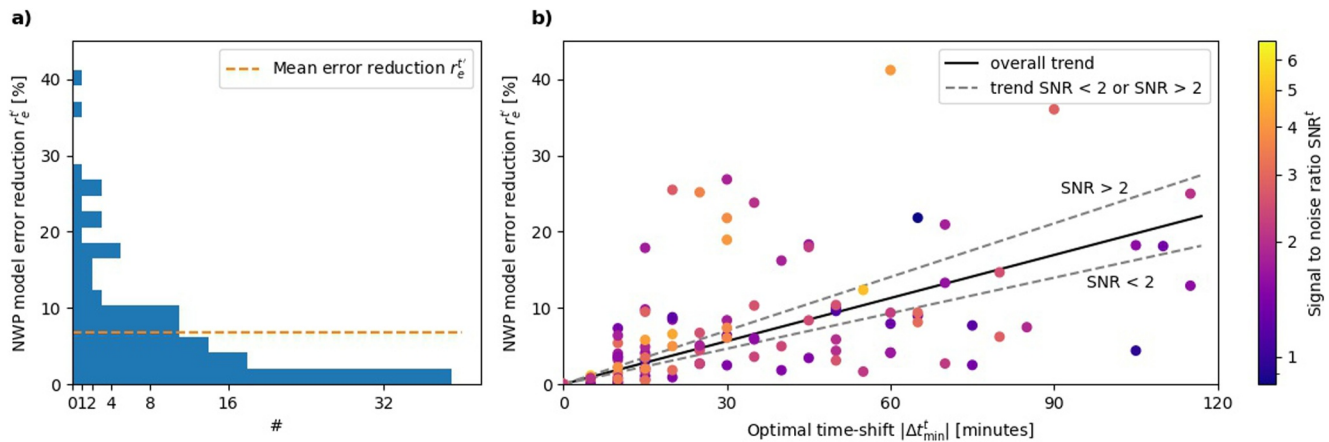


Figure 8. Model error reduction r_e^t distribution. (a) Distribution of r_e^t for all epoch, with a mean error reduction of 7%. This shows that for most cases an error reduction could be realized with a limited number of cases with large model error reductions up to 40% (b) Model error reduction r_e^t as a function of the absolute value of the optimal time-shift $|\Delta t_{\sigma,min}^t|$. This shows that there is a clear relation between the found optimal time-shift and error reduction. The color of the dots indicate the SNR values, and the dotted lines the error reduction with low and high SNR values. This shows that the application of a time-shift is more advantageous if InSAR delay patterns coincide well with the NWP model.

Instead, NWP model error improvements are strongly dependent on the weather situation of individual cases. Especially cases where weather fronts are present show large improvements, because the movement of these fronts is strongly related to advection and can therefore be correlated with a model time-shift.

However, other weather types show less or no correlation with time-shifts. For example, cases with strong local convection are mainly driven by non-linear effects, which cannot be captured by advection. Moreover, the

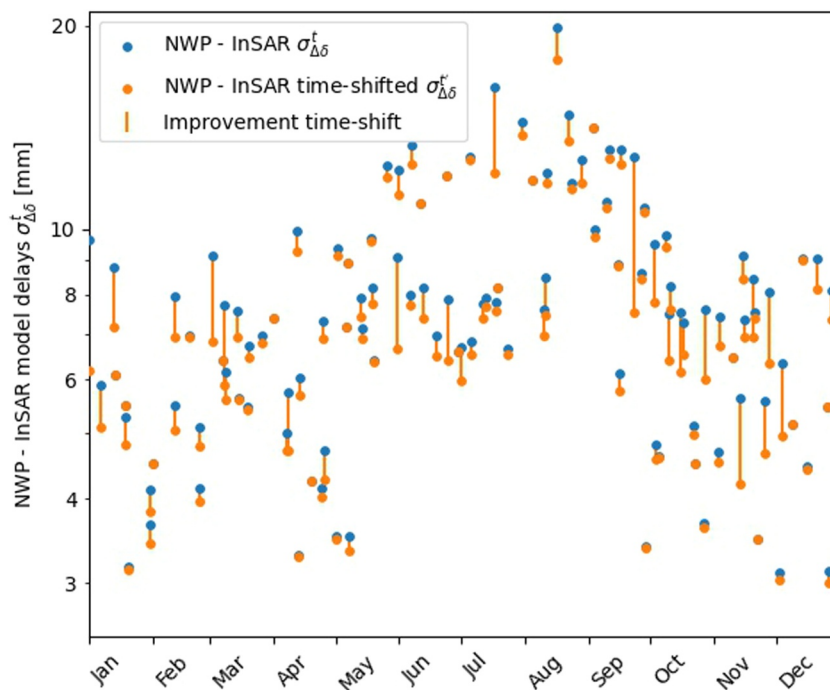


Figure 9. Difference in delay between InSAR and NWP model data, per epoch, expressed as standard deviation at time of the year over the full study period. In blue, the original values $\sigma_{\Delta\delta}^t$. In orange, the time-shifted values $\sigma_{\Delta\delta}^t$ with $t' = t + \Delta t_{\sigma,min}^t$. Note the logarithmic vertical axis. Larger differences between InSAR and NWP model data are observed in summer, due to higher temperatures and specific humidity (KNMI, 2023a). The orange lines stress the level of improvement as a consequence of an estimated time-shift.

locations of these convective systems are not related to the timing of the model but by local weather conditions that drive the development of convective systems. The last example of Figure 3 is a good example of such a case. While the model shows two areas with high delay in the north and middle of the image, the data shows two much smaller areas further to the south-west, which cannot be resolved using a time-shift. Because it is not possible to align these convective systems with time-shift these cases will almost always result in estimates with multiple minima and maxima that are removed from the analysis as unreliable, see Section 3.2. Other examples where the use of time-shift does not yield reliable result are winter cases where the weather is calm, which results in minimal horizontal variations in de delay, or cases where the ground is covered with snow, which results unreliable InSAR delay measurements. Fortunately, these cases generally result in a estimated optimal time-shift of -120 or 120 min, which also leads to the removal of these cases.

Therefore, this method should mainly be applied in cases with frontal systems as they can benefit most from applying time-shifts. Especially cold fronts will give accurate time-shifts, due to the abrupt temperature and water vapor differences, which leads to a clear jump in delay values.

4. Conclusion

The use of time-shifts estimated using satellite InSAR data can be a very effective addition to existing assimilation techniques, leading to model error reductions of up to 40% in cases where weather fronts are present, while in most other cases the model error reduction could reach up to 10%. In particular cases with cold fronts showed strong improvements. High model error reductions are therefore not specific for the summer or winter season, although the absolute model errors are larger during the summer season due higher PWV values. Likely, this is because these fronts show large scale features with strong water vapor variations and a clear time component due to the movement of the front. Other cases with very local convective systems or calm weather types, which are either short lived or lacking clear water vapor patterns, show therefore only minimal improvement. Finally, the cases with large model error reductions are already relatively well-described by the NWP model, which suggests that potential model improvements due to InSAR become larger with better model quality.

This shows that under the right conditions time-shifts can potentially lead to large model improvements and should therefore be considered as an additional component of data assimilation methods.

Data Availability Statement

The used InSAR images are derived from Sentinel-1 SLC data, which is freely available from the Copernicus hub (ESA, 2023). The used NWP model data of the Harmonie-Arome model is available from the website of the Royal Dutch Meteorological Service (KNMI, 2023b). Most data processing is done using the Radar Interferometric Parallel Processing Lab (RIPPL) software (Mulder, 2023), which includes a processing module to compare InSAR and NWP model data. To study areas outside the Netherlands using the same approach NWP model data from the ERA5 model (CDS, 2023) can be used, which can also be downloaded and processed by the RIPPL software.

References

- Alduchov, O., & Eskridge, R. (1997). *Improved Magnus' form approximation of saturation vapor pressure (Tech. Rep.)*. Oak Ridge Operations. <https://doi.org/10.2172/548871>
- Alshawaf, F., Hinz, S., Mayer, M., & Meyer, F. J. (2015). Constructing accurate maps of atmospheric water vapor by combining interferometric synthetic aperture radar and GNSS observations. *Journal of Geophysical Research: Atmospheres*, *120*(4), 1391–1403. <https://doi.org/10.1002/2014JD022419>
- Barkmeijer, J., Lindskog, M., Gustafsson, N., Bojarova, J., Azad, R., Monteiro, I., et al. (2021). HARMONIE-AROME 4D-VAR. *ALADIN-HIRLAM newsletter* (16). Retrieved from <https://www.umr-cnrm.fr/aladin/IMG/pdf/nl16.pdf>
- Bengtsson, L., Andrae, U., Aspelien, T., Batrak, Y., Calvo, J., Rooy, W. d., et al. (2017). The HARMONIE-AROME model configuration in the ALADIN-HIRLAM NWP system. *Monthly Weather Review*, *145*(5), 1919–1935. <https://doi.org/10.1175/MWR-D-16-0417.1>
- Bevis, M., Businger, S., Chiswell, S., Herring, T. A., Anthes, R. A., Rocken, C., & Ware, R. H. (1994). GPS meteorology: Mapping Zenith wet delays onto precipitable water. *Journal of Applied Meteorology*, *33*(3), 379–386. [https://doi.org/10.1175/1520-0450\(1994\)033<0379:GMMZWD>2.0.CO;2](https://doi.org/10.1175/1520-0450(1994)033<0379:GMMZWD>2.0.CO;2)
- Bevis, M., Chiswell, S., Businger, S., Herring, T. a., & Bock, Y. (1996). Estimating wet delays using numerical weather analyses and predictions. *Radio Science*, *31*(3), 477–487. <https://doi.org/10.1029/96RS00008>
- CDS. (2023). Climate data Store [Dataset]. *European Centre for Medium-Range Weather Forecasts (ECMWF)*. Retrieved from <https://cds.climate.copernicus.eu>
- Courtier, P., Andersson, E., Heckley, W., Vasiljevic, D., Hamrud, M., Hollingsworth, A., et al. (1998). The ECMWF implementation of three-dimensional variational assimilation (3D-var). I: Formulation. *Quarterly Journal of the Royal Meteorological Society*, *124*(550), 1783–1807. <https://doi.org/10.1002/qj.49712455002>

Acknowledgments

This project was enabled by the Dutch Research Council (NWO) under project ALW-GO/14-39.

- Danklmayer, A., & Chandra, M. (2009). Precipitation induced signatures in SAR images. In *2009 3rd European conference on antennas and propagation* (pp. 3433–3437).
- Davis, J. L., Herring, T. A., Shapiro, I. I., Rogers, A. E. E., & Elgered, G. (1985). Geodesy by radio interferometry: Effects of atmospheric modeling errors on estimates of baseline length. *Radio Science*, *20*(6), 1593–1607. <https://doi.org/10.1029/RS020i006p01593>
- De Haan, S. (2008). *Meteorological applications of a surface network of Global Positioning System receivers*. [Unpublished Doctoral Dissertation]. Wageningen University.
- De Haan, S. (2013). Assimilation of GNSS ZTD and radar radial velocity for the benefit of very-short-range regional weather forecasts. *Quarterly Journal of the Royal Meteorological Society*, *139*(677), 2097–2107. <https://doi.org/10.1002/qj.2087>
- Elgered, G., Davis, J. L., Herring, T. A., & Shapiro, I. I. (1991). Geodesy by radio interferometry: Water vapor radiometry for estimation of the wet delay. *Journal of Geophysical Research*, *96*(B4), 6541–6555. <https://doi.org/10.1029/90JB00834>
- ESA. (2023). Copernicus data space ecosystem [Dataset]. *Copernicus*. Retrieved from <https://dataspace.copernicus.eu/>
- Gomba, G., Parizzi, A., De Zan, F., Eineder, M., & Bamler, R. (2016). Toward operational compensation of ionospheric effects in SAR interferograms: The split-spectrum method. *IEEE Transactions on Geoscience and Remote Sensing*, *54*(3), 1446–1461. <https://doi.org/10.1109/TGRS.2015.2481079>
- Gomba, G., Rodríguez Gonzalez, F., & De Zan, F. (2017). Ionospheric phase screen compensation for the Sentinel-1 TOPS and ALOS-2 ScanSAR modes. *IEEE Transactions on Geoscience and Remote Sensing*, *55*(1), 223–235. <https://doi.org/10.1109/TGRS.2016.2604461>
- Gustafsson, N., Janjić, T., Schraff, C., Leuenberger, D., Weissmann, M., Reich, H., et al. (2018). Survey of data assimilation methods for convective-scale numerical weather prediction at operational Centres. *Quarterly Journal of the Royal Meteorological Society*, *144*(713), 1218–1256. <https://doi.org/10.1002/qj.3179>
- Hanssen, R. F. (2001). *Radar interferometry: Data interpretation and error analysis*. [Unpublished Doctoral Dissertation]. Delft University of Technology.
- Hanssen, R. F., Weckwerth, T. M., Zebker, H. A., & Klees, R. (1999). High-resolution water vapor mapping from interferometric radar measurements. *Science*, *283*(5406), 1297–1299. <https://doi.org/10.1126/science.283.5406.1297>
- Heublein, M., Alshawaf, F., Erdnüb, B., Zhu, X. X., & Hinz, S. (2019). Compressive sensing reconstruction of 3D wet refractivity based on GNSS and InSAR observations. *Journal of Geodesy*, *93*(2), 197–217. <https://doi.org/10.1007/s00190-018-1152-0>
- Huang, L., Fang, X., Zhang, T., Wang, H., Cui, L., & Liu, L. (2022). Evaluation of surface temperature and pressure derived from MERRA-2 and ERA5 reanalysis datasets and their applications in hourly GNSS precipitable water vapor retrieval over China. *Geodesy and Geodynamics*, *14*(2), 111–120. <https://doi.org/10.1016/j.geog.2022.08.006>
- Ishimaru, A. (1978). *Wave propagation and scattering in random media*. Elsevier. <https://doi.org/10.1016/B978-0-12-374701-3.X5001-7>
- KNMI. (2023a). Daggegevens van het weer in Nederland [Dataset]. *Royal Netherlands Meteorological Institute (KNMI)*. Retrieved from <http://www.knmi.nl/klimatologie/dagegevens/download.html>
- KNMI. (2023b). KNMI data platform [Dataset]. *Royal Netherlands Meteorological Institute (KNMI)*. Retrieved from <https://dataplatfom.knmi.nl/dataset/harmonie-arome-cy43-p5-1-0>
- Mateus, P., Catalao, J., & Nico, G. (2017). Sentinel-1 interferometric SAR mapping of precipitable water vapor over a country-spanning area. *IEEE Transactions on Geoscience and Remote Sensing*, *55*(5), 2993–2999. <https://doi.org/10.1109/TGRS.2017.2658342>
- Mateus, P., & Miranda, P. M. (2022). Using InSAR data to improve the water vapor distribution downstream of the core of the south American low-level Jet. *Journal of Geophysical Research: Atmospheres*, *127*(7). <https://doi.org/10.1029/2021JD036111>
- Mateus, P., Miranda, P. M., Nico, G., & Catalao, J. (2021). Continuous multitrack assimilation of sentinel-1 precipitable water vapor maps for numerical weather prediction: How far can we go with current InSAR data? *Journal of Geophysical Research: Atmospheres*, *126*(3). <https://doi.org/10.1029/2020JD034171>
- Mateus, P., Miranda, P. M. A., Nico, G., Catalão, J., Pinto, P., & Tomé, R. (2018). Assimilating InSAR maps of water vapor to improve heavy rainfall forecasts: A case study with two successive storms. *Journal of Geophysical Research: Atmospheres*, *123*(7), 3341–3355. <https://doi.org/10.1002/2017JD027472>
- Mateus, P., Tome, R., Nico, G., & Catalao, J. (2016). Three-Dimensional variational assimilation of InSAR PWV using the WRFDA model. *IEEE Transactions on Geoscience and Remote Sensing*, *54*(12), 7323–7330. <https://doi.org/10.1109/TGRS.2016.2599219>
- Meyer, F. J. (2011). Performance requirements for ionospheric correction of low-frequency SAR data. *IEEE Transactions on Geoscience and Remote Sensing*, *49*(10), 3694–3702. <https://doi.org/10.1109/TGRS.2011.2146786>
- Miranda, P. M. A., Mateus, P., Nico, G., Catalão, J., Tomé, R., & Nogueira, M. (2019). InSAR meteorology: High-resolution geodetic data can increase atmospheric predictability. *Geophysical Research Letters*, *46*(5), 2949–2955. <https://doi.org/10.1029/2018GL081336>
- Mulder, G. (2023). Radar interferometric Parallel processing Lab [Software]. *Department of Geosciences and Remote Sensing, Delft University of Technology*. Retrieved from <https://github.com/TU-DelftGeodesy/RIPPL>
- Mulder, G., Van Leijen, F. J., Barkmeijer, J., De Haan, S., & Hanssen, R. F. (2022). Estimating single-epoch integrated atmospheric refractivity from InSAR for assimilation in numerical weather models. *IEEE Transactions on Geoscience and Remote Sensing*, *60*, 1–12. <https://doi.org/10.1109/TGRS.2022.3177041>
- Palmer, T. (2019). The ECMWF ensemble prediction system: Looking back (more than) 25 years and projecting forward 25 years. *Quarterly Journal of the Royal Meteorological Society*, *145*(S1), 12–24. <https://doi.org/10.1002/qj.3383>
- Skamarock, W. C. (2004). Evaluating mesoscale NWP models using kinetic energy spectra. *Monthly Weather Review*, *132*(12), 3019–3032. <https://doi.org/10.1175/MWR2830.1>
- Smith, E., & Weintraub, S. (1953). The constants in the equation for atmospheric refractive index at radio frequencies. *Journal of Research of the National Bureau of Standards*, *50*(1), 39. <https://doi.org/10.6028/jres.050.006>
- Thayer, G. D. (1974). An improved equation for the radio refractive index of air. *October*, *9*(10), 803–807. <https://doi.org/10.1029/rs009i010p00803>
- WMO. (2018). *Guide to instruments and methods of observation (WMO No. 8)* (Vol. I). WMO.
- Yague-Martinez, N., Prats-Iraola, P., Rodríguez Gonzalez, F., Bricc, R., Shau, R., Geudtner, D., et al. (2016). Interferometric processing of Sentinel-1 TOPS data. *IEEE Transactions on Geoscience and Remote Sensing*, *54*(4), 2220–2234. <https://doi.org/10.1109/TGRS.2015.2497902>